



RESEARCH ARTICLE

An Overhauser-enhanced-MRI platform for dynamic free radical imaging *in vivo*

David E. J. Waddington^{1,2,3} | Mathieu Sarracanie^{1,2,4} | Najat Salameh^{1,2,4} | Fanny Herisson⁵ | Cenk Ayata^{4,5} | Matthew S. Rosen^{1,2,4}¹A. A. Martinos Center for Biomedical Imaging, 149 Thirteenth St., Charlestown, MA 02129, USA²Department of Physics, Harvard University, 17 Oxford St, Cambridge, MA 02138, USA³ARC Centre of Excellence for Engineered Quantum Systems, School of Physics, The University of Sydney, Sydney, NSW 2006, Australia⁴Harvard Medical School, 25 Shattuck St., Boston, MA 02115, USA⁵Stroke and Neurovascular Regulation Laboratory, Departments of Radiology and Neurology, Massachusetts General Hospital/Harvard Medical School, Charlestown, MA 02129, USA**Correspondence**David E. J. Waddington, A. A. Martinos Center for Biomedical Imaging, 149 Thirteenth St., Charlestown, MA 02129, USA.
Email: waddington.david@gmail.com**Funding information**

DOD DMRDP, Grant/Award Number: W81XWH-11-2-0076 and DM09094; Australian-American Fulbright Commission: ANSTO Award; Swiss National Science Foundation, Grant/Award Number: P3000P2 147768

Overhauser-enhanced MRI (OMRI) is an electron-proton double-resonance imaging technique of interest for its ability to non-invasively measure the concentration and distribution of free radicals. *In vivo* OMRI experiments are typically undertaken at ultra-low magnetic field (ULF), as both RF power absorption and penetration issues—a consequence of the high resonance frequencies of electron spins—are mitigated. However, working at ULF causes a drastic reduction in MRI sensitivity. Here, we report on the design, construction and performance of an OMRI platform optimized for high NMR sensitivity and low RF power absorbance, exploring challenges unique to probe design in the ULF regime. We use this platform to demonstrate dynamic imaging of TEMPOL in a rat model. The work presented here demonstrates improved speed and sensitivity of *in vivo* OMRI, extending the scope of OMRI to the study of dynamic processes such as metabolism.

KEYWORDS

free radical imaging, Overhauser-enhanced MRI (OMRI), RF coil design, ultra-low magnetic field

1 | INTRODUCTION

Free radicals play crucial roles in the maintenance of tissue health and in the pathogenesis of diseases including diabetes,¹ ischemia-reperfusion injuries² and cancer.³ Improvements to accurate diagnosis and appropriate treatment of diseases in which free radicals play a role require the development of non-invasive methods for mapping the distribution of free radicals *in vivo*. Electron paramagnetic resonance (EPR) is the gold standard of direct free radical detection, enabling unambiguous identification of the unpaired electrons inherent to radical species, but short electronic spin-spin lifetimes (T_{2e}) limit resolution in EPR-based imaging approaches.^{4,5} Overhauser-enhanced MRI (OMRI) overcomes the resolution limits of EPR imaging by indirectly imaging free radicals with high-resolution MRI.⁶⁻⁸ In OMRI, the Overhauser effect is used to transfer large spin polarizations from electronic radical species to dipolar-coupled ¹H nuclei, with subsequent ¹H MRI used to image the free radical distribution via enhanced ¹H spin polarizations.

Abbreviations used: ACA, anterior cerebral artery; AG, Alderman-Grant; AT, total acquisition time; bSSFP, balanced steady-state free precession; EPR, electron paramagnetic resonance; ICA, internal carotid artery; MAG, modified Alderman-Grant; NA, number of averages; OMRI, Overhauser-enhanced MRI; PE, phase encode; RO, readout; ROI, region of interest; SAR, specific absorbance rate; SF, sampling factor; SNR, signal-to-noise ratio; TEMPOL, 4-hydroxy-TEMPO; ULF, ultra-low magnetic field

While progress in OMRI has seen free radicals used as bioprobes of tissue oxygenation, metabolism and viscosity,⁹⁻¹³ sensitivity limits have prevented widespread use. The sensitivity of OMRI is limited in comparison with clinical MRI, as the high gyromagnetic ratio of electrons (28 GHz/T) means that OMRI is typically performed at ultra-low magnetic fields (ULF, <10 mT) to reduce the specific absorbance rate (SAR) to safe levels during the application of RF EPR saturation pulses.^{14,15} Overcoming the tradeoff between SAR and NMR sensitivity has thus been a focus of OMRI development.¹⁶ OMRI probes based on single-loop surface coil resonators minimize SAR by restricting the size of the EPR coil but necessarily have an inhomogeneous Overhauser enhancement profile due to spatial variation in B_{1e} .^{17,18} Volume resonators built for EPR saturation can yield high B_{1e} homogeneity, but compromises often need to be made to minimize SAR and maintain the quality factor (Q-factor) of the NMR detection coil.¹⁸⁻²⁰ With another approach, field-cycled OMRI, the applied magnetic field is rapidly ramped to allow EPR saturation at ULF followed by high-efficiency NMR acquisition at near-clinical field strengths.¹⁴ These field-cycled scanners improve OMRI sensitivity at the cost of significantly more complex hardware, but are slowed by the need to refresh the Overhauser-enhanced signal between acquisitions.

Recent advances in balanced steady-state free precession (bSSFP) MRI sequences at ULF have increased the speed and sensitivity of OMRI,²¹⁻²⁵ raising the possibility of *in vivo* radical imaging with high temporal resolution. A stable nitroxide radical of interest for dynamic tracking with OMRI is TEMPOL (4-hydroxy-TEMPO). TEMPOL is a neuroprotective antioxidant²⁶ whose permeability across the blood-brain barrier increases in cases of oxidative stress.^{27,28} As TEMPOL reduction has previously been used to monitor redox status in animal models, dynamic tracking of exogenously administered TEMPOL may prove a valuable tool for monitoring neurological diseases in which oxidative stress plays a key role, such as ischemia-reperfusion injury and Alzheimer's disease.²⁹

Here we report on an OMRI platform designed for dynamic imaging of TEMPOL in a rat model at ULF. Simulations and experimental results are presented to evaluate the performance of a custom OMRI probe based on a modified Alderman-Grant (MAG) resonator and designed for high sensitivity, enhancement, homogeneity and low SAR. Further, we leverage a highly efficient 3D bSSFP OMRI sequence to image TEMPOL *in vitro* at concentrations as low as 10 μM . We conclude this work with an *in vivo* demonstration of our platform, presenting brain images of TEMPOL in a rat model. This platform will enable tracking of exogenously administered radicals to study the role of oxidative stress in neurological diseases. The advances described here will also be of broader value in the design of OMRI platforms for the tracking of targeted radical species and the imaging of biological processes such as metabolism.

2 | MATERIALS AND METHODS

2.1 | OMRI scanner

Experiments were performed in a custom-built, ULF MRI scanner consisting of a biplanar 6.5 mT electromagnet with biplanar gradients (Figure 1A).^{23,30} A Redstone NMR Spectrometer (Tecmag, Houston, TX, USA) was used for data acquisition, RF pulse generation and gradient control. A 100 W CW amplifier (BT00100- DeltaB-CW) was used for EPR irradiation at 141 MHz and a 500 W pulsed power amplifier (BT00500-AlphaS) for NMR pulses at 276 kHz (TOMCO Technologies, Stepney, SA, Australia). Techron 7780 gradient amplifiers (Elkhart, IN, USA) were used to drive orthogonal gradients to a maximum strength of 1 mT m^{-1} .

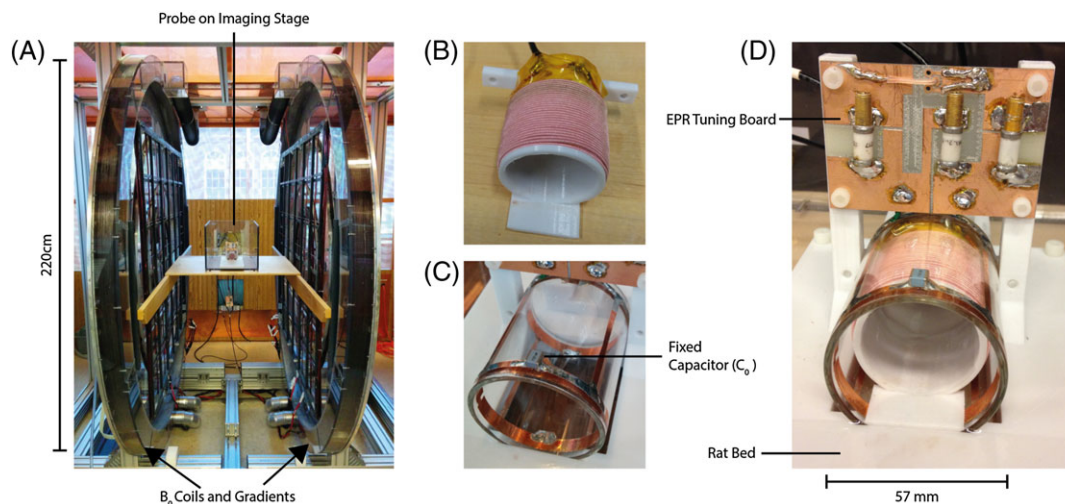


FIGURE 1 Hardware for OMRI at ULF. A, Ultra-low field 6.5 mT MRI scanner with rat probe on the imaging table between electromagnet and gradient coils. B, NMR solenoid coil wound on a polycarbonate former. The coil is tuned and matched to 276 kHz with an external resonator board (not shown). C, MAG EPR (141 MHz) resonator. D, NMR/EPR rat head probe assembly. High-voltage variable capacitors on EPR tuning board are used for fine-tuning and matching

The custom-built OMRI probe shown in Figure 1 was used for all imaging. This probe consists of an internal solenoid used for transmit and receive of the ^1H NMR signal and an external, MAG resonator used for EPR saturation. The design of this probe is now described in detail.

2.2 | NMR design

In ULF MRI, noise from the intrinsic resistance of the NMR receive coil dominates over sample noise.³¹ Hence, for optimal sensitivity, the Q-factor of the NMR coil should be increased to the point that the resonator bandwidth is slightly larger than the required imaging bandwidth.³² The required bandwidth in our probe is given by $\Delta f_{\text{im}} = \gamma_{\text{H}} G_{\text{max}} \Delta d = 1.9$ kHz, where γ_{H} is the proton Larmor frequency (42.576 MHz T⁻¹), G_{max} is the maximum gradient strength (1 mT m⁻¹) and Δd is the maximum desired field of view (45 mm).

A 35 mm long solenoidal NMR coil was wound on a 3D-printed 45 mm diameter polycarbonate former using 5/39/42 litz wire (New England Wire Technologies, Lisbon, NH, USA), as shown in Figure 1B. The specifications of this Litz wire were chosen to minimize AC resistance at 276 kHz. An external resonator board was used to parallel-tune and series-match the solenoid to 276 kHz with non-magnetic ceramic chip capacitors (Voltronics, Cazenovia, NY, USA). Construction with 85 turns of litz wire in a double layer gave an unloaded NMR resonator bandwidth of 2.5 kHz ($Q = 109$). Coil dimensions were chosen to maximize the fill factor when imaging a rat's head. The NMR geometric fill factor, and resulting ^1H receive sensitivity, was prioritized over the EPR fill factor, as lower EPR fill factors can be overcome by using higher EPR transmit power.

2.3 | EPR design

Effective OMRI probe design maximizes the B_{1e} -field that can be applied while minimizing the SAR that arises from inductive and dielectric heating effects during EPR saturation. Inductive power deposition occurs when the alternating B_{1e} -field induces currents that dissipate energy in a conductive sample, and is proportional to $\omega_e^2 B_{1e}^2$.³³ Dielectric power deposition results from a quasi-frictional force, as electric dipole moments of molecules in the sample align with the alternating electric field E in the EPR resonator, and is proportional to $\omega_e E^2 \epsilon''(\omega_e)$, where $\epsilon''(\omega_e)$ is the imaginary component of the dielectric constant of the sample.

To reduce both heating effects, the EPR frequency ω_e is minimized by driving the lowest-frequency transition of the TEMPOL spectral triplet, which is at 141 MHz in our ULF scanner (see Supplementary Figure 1 for Overhauser enhancement spectra identifying the three resonant lines). We also used a 70 mm length, 57 mm diameter and 2.4 mm thick piece of Pyrex tubing (Chemglass, Vineland, NJ, USA) as the EPR former for its close fit around the NMR coil (see Fig 1C), as maximizing the EPR fill factor confines E - and B_{1e} -fields, and resultant heating, to the region of interest (ROI).

The Alderman-Grant (AG) resonator, originally designed to reduce heating of conductive samples in proton-decoupled NMR experiments at high magnetic fields,^{34,35} is a popular choice for minimizing SAR. Compared with alternatives such as a saddle coil, capacitive segmentation of the AG resonator reduces sample losses caused by the E -field, as voltage only accumulates over half the inductance before reversal at the segmentation capacitor.³⁶ Further, quadrupolar symmetry reduces the average value of the E -field in the sample.

Here, we construct a modified MAG resonator by affixing two pieces of 0.07 mm thick adhesive copper tape (3M, Maplewood, MN, USA) to the Pyrex EPR former along with four 12 pF bridging capacitors (Figure 1C). The MAG resonator is assembled around the NMR coil (Figure 1D). The copper tape is shaped such that the MAG resonator has the geometry of an AG resonator with additional split guard rings and "windows" in the copper foils that form the sides of the resonator, as is shown schematically in Figure 2A. B_{1e} is oriented in the vertical direction (i.e. perpendicular to the coronal plane for the rat), orthogonal to the axial B_{1H} of the solenoid. High-voltage variable capacitors (NMAJ40HV—Voltronics, Cazenovia, NY, USA), in a balanced series-match, parallel-tune configuration, are used to connect the resonator to the EPR drive amplifier. A conventional AG resonator with the same geometry and internal guard rings made from continuous loops of copper tape was also constructed for comparison.

Finite element analysis simulations of EPR resonators were performed in COMSOL Multiphysics (COMSOL, Burlington, MA, USA). Copper foils were simulated as perfect electrical conducting surfaces (a 3D rendered model is included in Supplementary Figure 2). Simulated resonators were tuned to 141 MHz with fixed capacitors modeled as lumped elements. Field values were normalized to 1 mT B_{1e} -field in the center of each resonator. In Figure 3 the NMR coil was modeled as a 40-turn helix with a perfect electrically conducting surface.

2.4 | Overhauser-enhanced MRI

Imaging was performed with a 3D OMRI bSSFP sequence that has been described previously.²¹ The efficiency of this sequence is improved over conventional OMRI sequences by using EPR saturation pulses coincident with phase encoding, allowing steady-state signal acquisition during more than one-third of the imaging time. Images were acquired with $T_E/T_R = 25.4/50.7$ ms, $T_{\text{PE}} = 16.3$ ms, readout time $T_{\text{RO}} = 17.1$ ms, a $128 \times 35 \times 11$ matrix (readout (RO) \times Phase Encode 1 (PE1) \times Phase Encode 2 (PE2)), and $1.1 \times 1.6 \times 8$ mm³ voxel size. A transmit power of 8 mW was used for NMR pulses 240 μs in length and a tip angle α of 70°. A sequence timing diagram is provided in Supplementary Figure 3. Phantom images were fully sampled (sampling factor (SF) = 1). Image reconstruction was performed via conventional Fourier reconstruction in MATLAB (MathWorks, Natick, MA, USA). The magnitude color scale in all images is normalized to the signal without Overhauser enhancement.

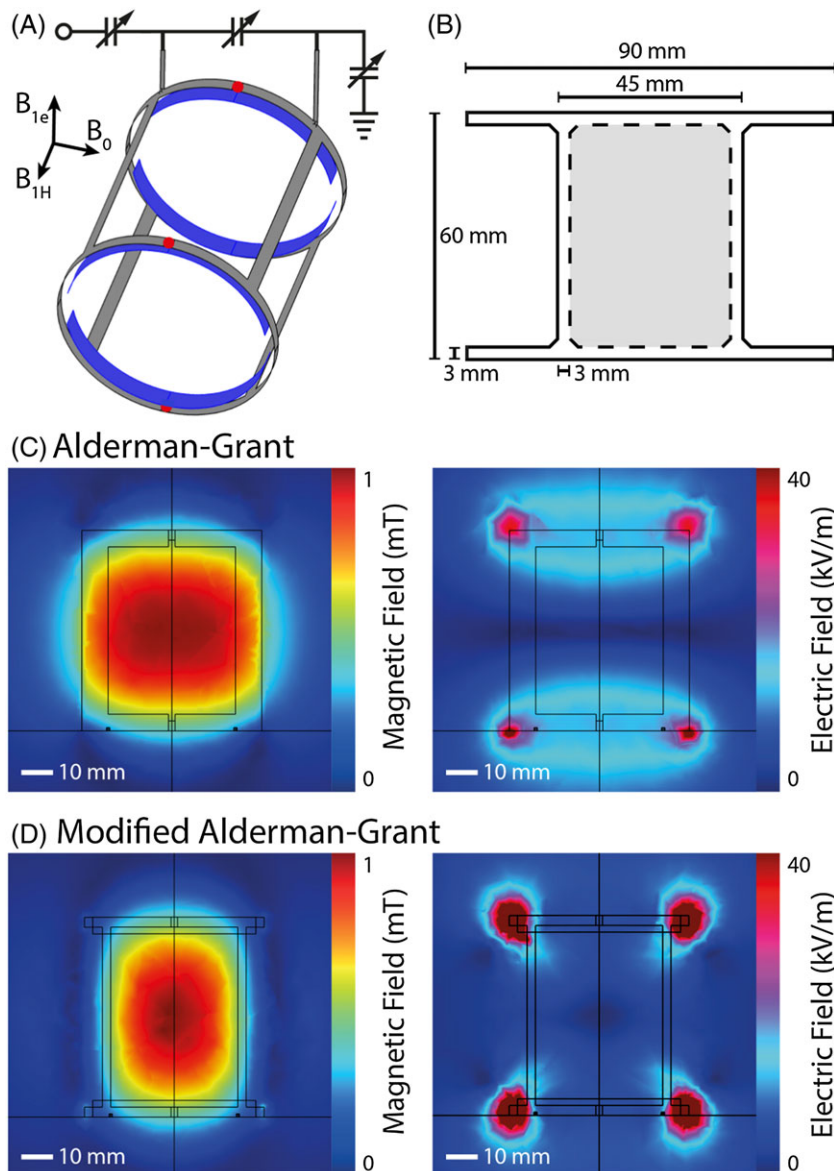


FIGURE 2 EPR resonator design. A, MAG resonator schematic. A traditional AG resonator with guard rings is modified by splitting the guard rings (shown in blue) and cutting windows in the sides of the slotted tube (shown in grey). Directions of mutually orthogonal B_0 , B_{1H} - and B_{1e} -fields are indicated. The fixed capacitor locations are marked in red (one is hidden from view). B, Shape and dimensions of copper foil pieces cut for EPR resonator. The region shaded in grey was removed to build the MAG resonator. C, Field simulations (B_{1e} —left, E —right) of AG resonator. D, Field simulations (B_{1e} —left, E —right) of MAG resonator

Probe homogeneity was measured with a 60 mL vial of 2 mM TEMPOL solution. An MRI reference image was acquired with no power supplied to the EPR resonator and a number of averages (NA) of 32. An OMRI image was then acquired with 15 W of EPR power and NA = 8.

TEMPOL sensitivity was tested using vials of various TEMPOL concentrations (shown in Figure 4). Reference images, with EPR pulses disabled, were acquired with an NA of 32, corresponding to an acquisition time (AT) of 9.5 min. Overhauser-enhanced images of a high-concentration phantom (Figure 4C) were acquired with 24 W of EPR power and NA = 1 (AT = 18 s). Overhauser-enhanced images of a low-concentration phantom (Figure 4D) were acquired with 24 W of EPR power and NA = 64 (AT = 19 min). Image signal-to-noise ratio (SNR) was measured as the average signal magnitude in an ROI divided by the standard deviation of the signal in a signal-free region at the edge of the field of view.

The longitudinal ^1H relaxivity (r_1) of TEMPOL in deionized water at 6.5 mT was found to be $0.67 \pm 0.07 \text{ mM}^{-1} \text{ s}^{-1}$ via T_1 inversion recovery measurements.

2.5 | Animal preparation

All experiments were performed in accordance with our institutional animal care and use committee guidelines.

Under anesthesia (2%-isoflurane), a 450g Sprague-Dawley male rat was prepared for TEMPOL injection while rectal temperature was continuously monitored. Buprenorphine 0.08 mg kg^{-1} was given subcutaneously 30 min before surgery. After dissection of the common carotid artery and

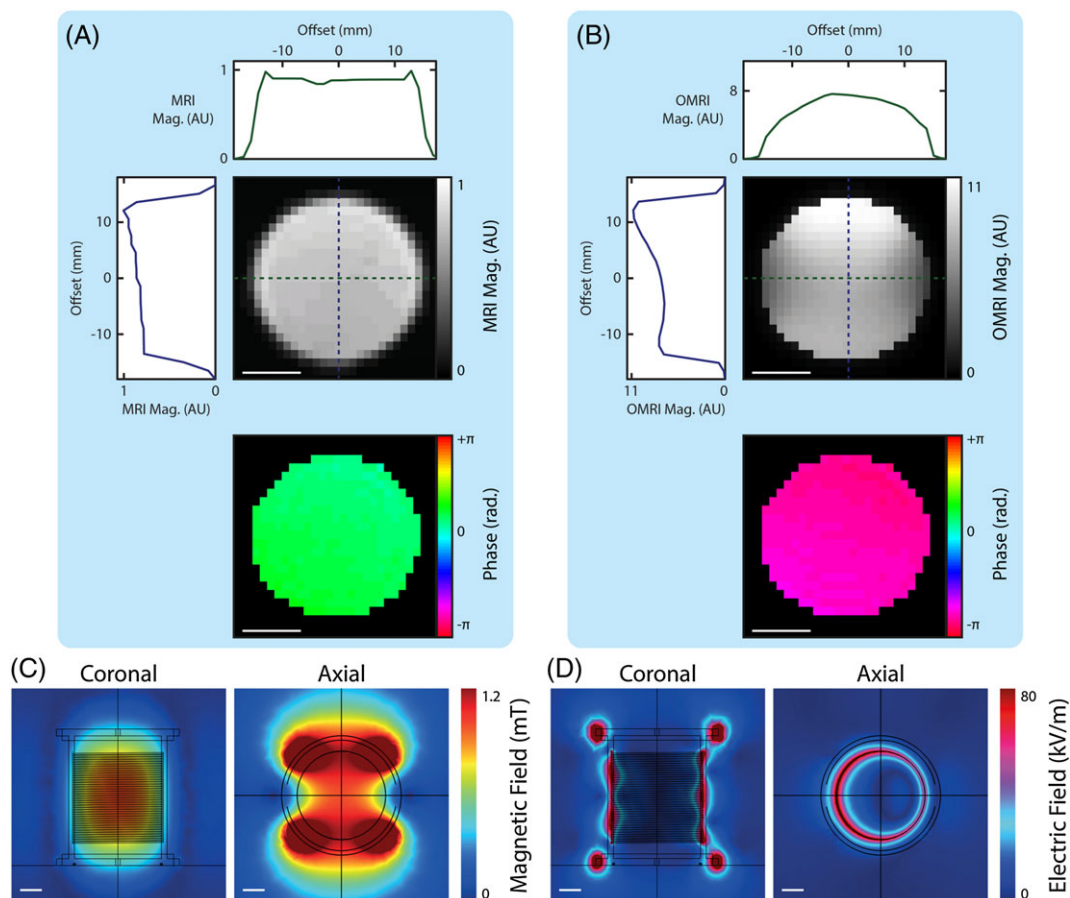


FIGURE 3 Overhauser enhancement in the complete NMR/EPR probe assembly. A, Axial slice of a 2 mM TEMPOL solution acquired with conventional bSSFP MRI. Magnitude (gray-scale) and phase (color-scale) images are displayed. The image was acquired with $NA = 32$, $SF = 1$ and EPR pulses disabled. Horizontal (green) and vertical (blue) line profiles show signal magnitude along the dotted lines. B, Axial slice of a 2 mM TEMPOL solution acquired with bSSFP OMRI. Magnitude (gray-scale) and phase (color-scale) images are displayed. The image was acquired with $NA = 8$, $SF = 1$ and 15 W of EPR power. Horizontal (green) and vertical (blue) line profiles show signal magnitude along the dotted lines. Magnitude color scales in A and B are normalized to a value of 1 for the unenhanced MRI signal. C, Simulations of the B_{1e} profile in coronal and axial cross-sections of our MAG resonator assembly. D, Simulated E-field profile of the MAG resonator assembly. Scale bars (white) are 10 mm in length

the carotid bifurcation, and ligation of the pterygopalatine artery and the external carotid artery, a polyethylene catheter (PE10) filled with 0.9% saline and 50 U mL^{-1} heparin, connected to a Genie Touch infusion pump (Kent Scientific, Torrington, CT, USA), was inserted via the external carotid and advanced into the right carotid artery bifurcation.

After surgery, the animal was transferred to the flat animal bed of the OMRI scanner. The NMR and EPR coils of the OMRI probe sit within a recessed slot in the animal bed. A sliding polycarbonate bite bar with integrated anesthesia nose cone was incorporated into the probe assembly to position the rodent in the isocenter of the scanner and to anesthetize it during imaging. A sealed glass sphere containing 2 mM TEMPOL was located on the contralateral side with respect to the catheter placement and used as a fiducial. An optical fiber temperature sensor (Osensa FTX-301-PWR, Burnaby, BC, Canada) was used for continuous rectal temperature measurement while the animal was in the scanner. Cardiac and respiratory rates, as well as oxygen saturation, were continuously monitored with a Model 1025T Monitoring and Gating System (Small Animal Instruments, Stony Brook, NY, USA).

2.6 | *In vivo* Overhauser-enhanced MRI

In vivo imaging was performed with the 3D bSSFP sequence described above, additionally accelerated by 50% random Gaussian undersampling in the phase encode direction ($SF = 0.5$) as described in Reference 21. A reference image was acquired using $NA = 30$, corresponding to $AT = 4.5$ min. Following the reference scan, 1 mL of 150 mM TEMPOL was injected into the internal carotid artery (ICA) over 2 min with the infusion pump. A dynamic OMRI sequence, consisting of 16 independent 3D OMRI acquisitions spaced at 15 s intervals, was started at the same time as the injection. Each OMRI scan had $NA = 1$ ($AT = 9$ s) and 24 W of power for EPR saturation pulses. Zero-filling was used for *in vivo* image processing to increase the acquired voxel resolution of $1.1 \times 1.6 \times 8 \text{ mm}^3$ to the interpolated resolution of $0.4 \times 0.4 \times 8 \text{ mm}^3$.

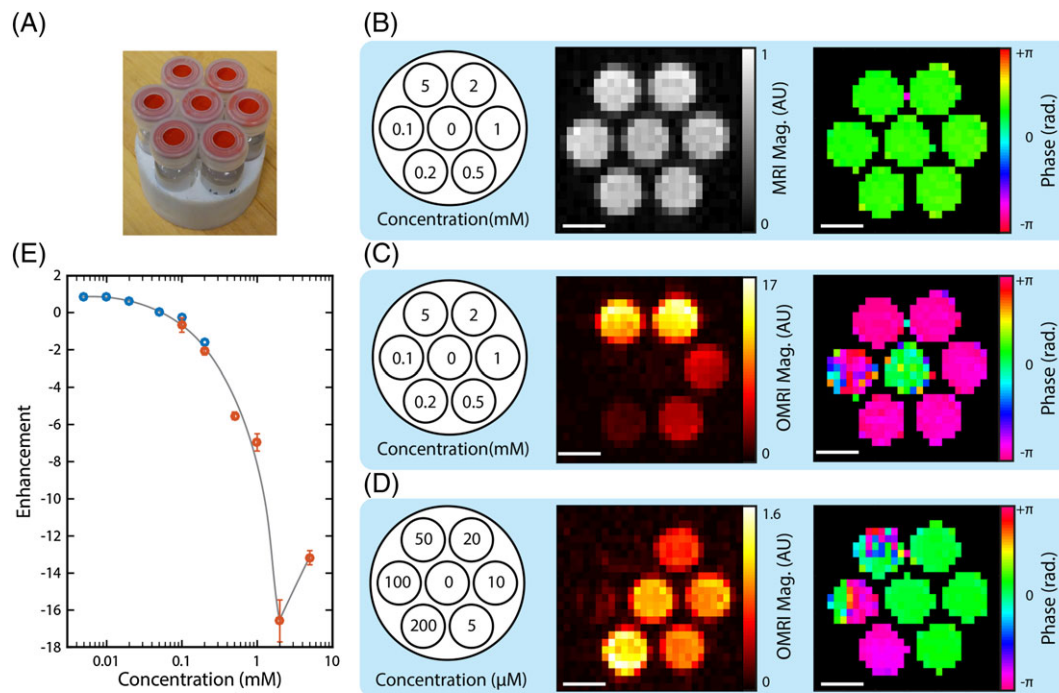


FIGURE 4 Sensitivity of TEMPOL imaging. A, Photograph of phantom containing 2 mL vials of TEMPOL. B, Conventional bSSFP MRI of a high-concentration TEMPOL phantom. The schematic diagram shows vial concentrations. The image was acquired with $NA = 32$, $SF = 1$ and EPR pulses disabled. C, OMRI of a high-concentration TEMPOL phantom. The schematic diagram shows vial concentrations. The image was acquired with $NA = 1$, $SF = 1$ and 24 W of EPR power. D, OMRI of a low-concentration TEMPOL phantom. The schematic diagram shows vial concentrations. The image was acquired with $NA = 64$, $SF = 1$ and 24 W of EPR power. All images were acquired at 6.5 mT. Scale bars (white) are 10 mm in length. Magnitude color scales in B, C and D are normalized to a value of 1 for the unenhanced MRI signal. E, Image enhancement as a function of TEMPOL concentration with 24 W of EPR power applied during acquisition. Markers indicate the mean enhancement of an ROI within each vial in images from B (red) and C (blue). Error bars indicate the standard deviation of enhancement within each ROI. Error bars are not shown where the error is smaller than the marker size

At the completion of the experiment, the animal was euthanized under deep anesthesia by cardiac perfusion followed by decapitation.

The *in vivo* RF power absorption was quantified by measuring the Q-factors of the loaded and unloaded EPR resonator via *s*-parameter (s_{21}) measurements taken with a network analyzer.

3 | RESULTS

3.1 | EPR resonator design

The unloaded NMR coil has a bandwidth of 2.1 kHz, which is broadened to 5.1 kHz upon assembly of the NMR coil with a conventional AG resonator with guard rings. This broadening corresponds to a 59% reduction in unloaded NMR Q-factor. Introducing small splits in the guard rings (see Figure 2A) reduces mutual inductance between the guard rings and the NMR coil, reducing the unloaded NMR bandwidth in the assembly by 0.5 kHz. Further modifying the AG resonator, by removing copper from the center of the resonator walls (see Figure 2B), minimizes losses occurring due to the proximity of wires in the NMR solenoid and the conducting planes that form the walls of the AG resonator, reducing the unloaded NMR bandwidth in the probe assembly to 2.9 kHz ($Q = 94$). Thus, these modifications give the OMRI probe with MAG resonator a near factor of two increase in NMR Q-factor when compared with the traditional AG resonator. The Q-factor of the unloaded EPR resonator is 30.5 at 141 MHz when measured in the complete probe assembly. We also note that, as the ^1H Larmor frequency is so low, broadening of the NMR resonance is dominated by coil resistance, and as such the NMR Q-factor is changed negligibly by sample loading of the probe.

To evaluate the changes in *E*-field and *B*-field that occur from resonator modifications, we performed finite element analysis simulations of an AG resonator and a MAG resonator, as shown in Figure 2(C,D). We find that in the center of an AG resonator there is high B_{1e} homogeneity and exclusion of the *E*-field, properties that have made the AG resonator popular for use in high-field bioimaging. Reduction of B_{1e} homogeneity in the new MAG resonator is minimized by removing the conducting walls of the AG resonator, which are the regions of lowest current density in the AG resonator.³⁵ We see that, in the B_0 direction, the orthogonal B_{1e} component falls to 50% of its maximum value at 26 mm from the center of the AG resonator, and at 20 mm from the center of the MAG resonator. Our simulations indicate that the split guard rings in the MAG resonator are effective at shielding

the large electric fields at the ends of the AG resonator. We note that the guard rings were split at the four points furthest from the fixed capacitors, where the E -field is expected to be at a minimum. Additionally, simulations also show that the B_{1e} homogeneity of the MAG resonator is improved by increasing the angle subtended between rungs in the B_{1e} direction. The MAG resonator homogeneity is increased at a subtended angle of 60° , the optimal angle for homogeneity in saddle coils,³⁷ but with much less effective E -field exclusion than seen in the resonator with the 90° subtended angle used here (supporting simulations are provided in Supplementary Figure 4).

3.2 | Probe performance

Images acquired without EPR, of a TEMPOL phantom (see Figure 3A), show that the NMR coil sensitivity is homogeneous across an axial slice, as would be expected from the axial symmetry of the solenoid. OMRI of the same phantom (Figure 3B) shows uniform inversion of MRI signal phase due to negative enhancement of the ^1H polarization via the Overhauser effect. There is spatial variation of Overhauser enhancement, with a reduction of intensity towards the horizontal edges of the field of view. Simulations of the EPR resonator that include a model of the NMR coil (Figure 3C) indicate that these hypointense areas of enhancement correspond to regions of lower B_{1e} . These simulations also show that inclusion of the NMR solenoid has little effect on B_{1e} -field, but does result in increased penetration of the E -field into the center of the imaging volume (Figure 3D) when compared with the simulations shown in Figure 2. This increased E -field penetration is to be expected, given the proximity of EPR and NMR coils, and close spacing of solenoid turns.

To test for *in vivo* changes in E - and B_{1e} -field profiles, simulations were also performed for the EPR probe when loaded with a 30 mm diameter sphere of the same conductivity and relative permittivity as brain grey matter.³⁸ These "*in vivo*" simulations showed E - and B_{1e} -field distributions nearly identical to those presented in Figure 3 (supporting data included in Supplementary Figure 5).

To assess the sensitivity of our OMRI probe to TEMPOL concentration, a phantom with vials containing high concentrations of TEMPOL (Figure 4A) was imaged with EPR pulses disabled, as shown in Figure 4B. No significant contrast is apparent between different vials in this reference image.

Afterwards, images were acquired with EPR pulses enabled, as shown in Figure 4C. Slices from this OMRI dataset show clear contrast between TEMPOL vials of different concentrations, with a maximum image enhancement of -17 observed in the 2 mM TEMPOL solution. Overhauser enhancement magnitude is reduced in the 5 mM solution, when compared with the 2 mM solution, due to broadening of the EPR line.³⁹ These image enhancements are relatively low compared with the enhancement values that can be observed in spectroscopic experiments with nitroxide radicals.^{21,39} Larger enhancement values would be observed with a higher B_{1e} that completely saturates the EPR line and with the use of a higher EPR duty cycle sequence. Reference and OMRI scans were also acquired from low-concentration vials of TEMPOL (OMRI scan shown in Figure 4D). The numerical enhancement within an ROI centered on each vial in Figure 4C and Figure 4D is shown in Figure 4E.

In our system at 24 W EPR power, below TEMPOL concentrations of 0.1 mM, the OMRI signal is no longer inverted by the Overhauser effect but instead is reduced in magnitude compared with the MRI signal. In this low-concentration regime, TEMPOL detection can be performed by comparison of the OMRI signal with the unenhanced MRI signal. Voxels of 50 μM , 20 μM , 10 μM and 5 μM TEMPOL in Figure 4D have average signal magnitudes of 0.05, 0.65, 0.85 and 0.88 respectively, compared with the unenhanced water value of 1. As the water vial has an SNR of 21 (noise = 0.05), voxels corresponding to 10 μM and 5 μM concentrations are just at the detection threshold with an OMRI signal change of two to three times the noise floor.

3.3 | *In vivo* overhauser-enhanced MRI

We begin our *in vivo* experiments by acquiring reference bSSFP MRI images of the rat head immediately following surgery (see Figure 5A). The 2 min, 1 mL injection of 150 mM TEMPOL is started and a 3D OMRI scan acquired every 15 s for a total of 4 min. These OMRI scans show negative ^1H signal enhancement in the ipsilateral hemisphere of the brain, as well as in the fiducial (see Figure 5B). Absolute signal enhancement decreases for the remainder of the scans (see Figure 5C) following the end of the injection. The mean signal in ROIs within ipsilateral and contralateral hemispheres of the brain show that signal changes are predominantly confined to the ipsilateral cerebral hemisphere (see Figure 5C,D), although the eye, and contralateral anterior cerebral artery (C-ACA) territory, which is supplied by a single confluent vessel contributed by the ipsilateral internal carotid, also appear to be labeled. Furthermore, the signal magnitude in the ipsilateral hemisphere peaks at the end of the injection, with the ^1H enhancement halving in the 2 min after injection. The 2 mM fiducial of TEMPOL displays an enhancement of -15.5 ± 0.7 , which is consistent with the enhancement expected from Figure 4E.

Rectal temperature remained at $37.8 \pm 0.2^\circ\text{C}$ throughout the experiment. The respiration rate remained within 64 ± 6 breaths per minute at all times, averaging 60 breaths per minute when the rat was at rest and increasing to a maximum of 70 breaths per minute during TEMPOL injection. The cardiac rate was steady at 310 ± 10 beats per minute when the rat was at rest and decreased to a minimum of 118 beats per minute during TEMPOL injection, likely due to the Cushing reflex. The cardiac rate recovered to 290 beats per minute by the end of the dynamic imaging sequence. An OMRI sequence run without TEMPOL injection showed no significant change in the monitored physiological parameters.

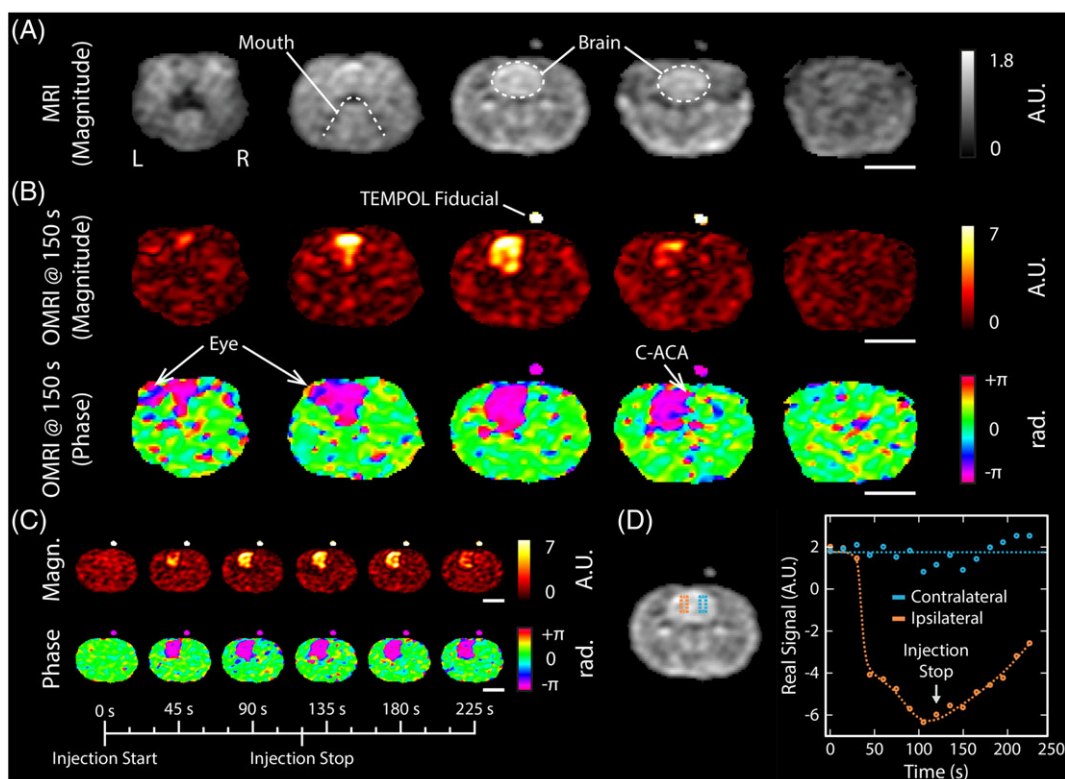


FIGURE 5 MRI and OMRI dynamics in a rat model. An anatomy scan was acquired with MRI before injection of 1 mL of 150 mM TEMPOL into the ICA over 2 min. The rat head was imaged with OMRI once every 15 s from the beginning of the injection. Each 9 s acquisition captured a full 11 slice dataset. A, The five central slices of the MRI anatomy scan. The anatomy scan was acquired with $NA = 30$, $SF = 0.5$ and EPR pulses disabled. B, OMRI bSSFP images acquired 150 s after the beginning of the TEMPOL injection. The five central slices are shown. Arrows indicate regions of the eye and C-ACA. C, Dynamic imaging of TEMPOL with OMRI during the injection. The OMRI signal from the central slice is shown at the indicated time points during and after injection. Magnitudes in all images are normalized to a value of 1 for the unenhanced MRI signal in the fiducial. OMRI scans in B and C were acquired with $NA = 1$, $SF = 0.5$ and 24 W of EPR power. The magnitude of the enhanced fiducial signal is 15.5 ± 0.7 . Note that the OMRI color-scale value is truncated to 7 in B and C to match the range of values in the *in vivo* data. D, The average real OMRI signal is plotted over time for ROIs in the ipsilateral hemisphere and contralateral hemisphere of the central slice. Scale bars (bottom right of subfigures, white) are 10 mm in length

3.4 | RF power absorption

Having demonstrated the *in vivo* use of our OMRI platform, we now quantify SAR, which is critical to determining limits on RF power use in future OMRI applications. The RF power absorbed during EPR pulses can be estimated from

$$P_{\text{abs}} = P_{\text{EPR}} \frac{\Delta Q}{Q_{\text{unloaded}}} \quad (1)$$

where P_{EPR} is the power to the EPR resonator, P_{abs} is the absorbed RF power, Q_{unloaded} is the Q-factor of the unloaded EPR resonator and ΔQ is the change in EPR resonator Q-factor on loading.³³ During *in vivo* experiments, P_{EPR} was 24 W and on loading with the rat $\Delta Q = 0.9$, giving $P_{\text{abs}} = 0.7$ W.

This power absorption gives a peak SAR of 1.6 W kg^{-1} when averaged over the mass of the entire rat (450 g) or 28 W kg^{-1} when averaged over the mass of the head (approximately 25 g). These SAR values apply for continuous EPR irradiation with 24 W of power. However, the EPR duty cycle over the dynamic imaging sequence is 40%, giving time-averaged SAR values of 0.6 W kg^{-1} when averaged over the entire rat and 11 W kg^{-1} when averaged over the head.

4 | DISCUSSION

The OMRI platform presented here has enabled dynamic *in vivo* imaging of TEMPOL with $1.1 \times 1.6 \times 8 \text{ mm}^3$ voxel size. Our imaging studies in phantoms demonstrate that the phase inversion of the ^1H MRI signal can be used to detect free radical presence at TEMPOL concentrations above 100 μM . Considering the sensitivity of phantom imaging in Figure 4D and, assuming that SNR scales with NA as \sqrt{NA} , we calculate that signal reduction from 50 μM TEMPOL is more than double the noise floor in our $NA = 1$ dynamic OMRI sequence, making 50 μM of TEMPOL the detection limit in an $NA = 1$ phantom image. To extrapolate this limit to the *in vivo* experiment we must consider that biological factors can reduce the imaging sensitivity. Hence, to estimate the TEMPOL concentration for the same enhancement in a biological environment we begin by noting that the Overhauser enhancement in an OMRI experiment is given by

$$e = 1 - \rho fs \quad (2)$$

where e is the enhancement, ρ is the coupling factor, f is the leakage factor and s is the saturation factor. It is expected that, for TEMPOL concentrations below a few millimolar, ρ and s will remain relatively constant in the *in vivo* experiment;³⁹ however, f depends strongly on TEMPOL concentration and the intrinsic spin-lattice relaxation time (T_{10}) of the animal tissue in the absence of free radicals, as given by

$$f = \frac{r_1 c T_{10}}{1 + r_1 c T_{10}} \quad (3)$$

At 6.5 mT we measure T_{10} of deionized water to be 3 s. Therefore, in our 50 μ M TEMPOL phantom, from Equation 3, the leakage factor is 0.09. To estimate the sensitivity of radical detection *in vivo*, we now calculate the TEMPOL concentration required in a rat brain to give the same enhancement as a 50 μ M TEMPOL phantom. The T_{10} of rat brain at 6.5 mT is approximately 180 ms.⁴⁰ Using Equation 3, we find that for an f of 0.09 in the rat brain the TEMPOL concentration should be 0.8 mM. Thus, the minimum TEMPOL concentration detectable in our dynamic $NA = 1$ *in vivo* images is of the order of 1 mM.

Having estimated the minimum detectable TEMPOL concentration in our $NA = 1$ *in vivo* images, we now estimate the peak TEMPOL concentration observed in the brain. The *in vivo* enhancement in the hemisphere ipsilateral to the TEMPOL injection reaches a maximum of -3.7 approximately 100 s after the beginning of the injection (see Figure 5D). This enhancement is similar to that expected from a 300 μ M aqueous solution of TEMPOL (see Figure 4E), which would have a leakage factor of $f = 0.38$ from Equation 3. Solving Equation 3 for this leakage factor and T_{10} of rat brain gives a TEMPOL concentration of $c = 5.1$ mM. Hence, we estimate that the lower limit of TEMPOL concentration in the ipsilateral hemisphere at peak enhancement is 5 mM. We note that, as the EPR linewidth of nitroxide radicals begins to broaden at these concentrations,³⁹ s will not be strictly constant as assumed here, and the true TEMPOL concentration could be significantly higher.

The long lifetime of enhancement in the ipsilateral hemisphere after injection suggests that TEMPOL may have entered the brain parenchyma. We believe that temporally resolved OMRI with our system will be useful for tracking redox status via the rate of appearance and disappearance of TEMPOL, especially in cases of oxidative stress where brain tissue may be permeable.²⁸

Our platform could also be of use for tracking radicals other than TEMPOL. Of particular interest is the imaging of custom nitroxides that can be targeted to mitochondria in order to reduce damage caused by reactive oxygen species^{41,42} or alternatively selectively delivered to tumors via the enhanced permeability and retention effect.⁴³ Beyond nitroxides, which have intrinsically broad hyperfine split EPR spectra,⁴⁴ the use of narrow, single-line radicals, such as trityl,^{9,45} would significantly increase the magnitude of the Overhauser enhancements observed in our system. However, we note that, as EPR saturation occurs during the phase encode step in our bSSFP OMRI sequence, the magnitude of the phase encode gradient is restricted by the radical linewidth.

We note that we have used relatively anisotropic voxels in this study ($1.1 \times 1.6 \times 8$ mm³) to enable whole brain coverage with a short scanning time whilst maintaining reasonably small in-plane resolution. More cubic voxels could be used to reduce partial volume effects in the axial direction at the expense of AT or in-plane resolution. Increasing B_{1e} , voxel size and AT are straightforward approaches to improving the concentration sensitivity of our platform. However, significantly increasing *in vivo* ATs would require the use of radicals with longer-term *in vivo* stability,⁴⁶ NMR sensitivity would be further improved by reducing coil noise, by implementing either a cryocooled coil⁴⁷ or active feedback.⁴⁸

Our custom OMRI probe has been designed for a high Q-factor in the NMR resonator and low SAR from the EPR resonator. While the homogeneity of our volume EPR resonator is highly favorable for imaging, as inductive heating scales as the fifth power of sample radius,⁴⁹ the use of surface EPR coils for B_{1e} confinement will be necessary for samples much larger than a rat's head.^{17,50,51}

In addition to the low-SAR design considerations of our EPR resonator, we have restricted ourselves to 24 W of incident EPR power to further minimize SAR concerns. Our peak SAR values, 1.6 W kg⁻¹ when averaged over the body and 28 W kg⁻¹ when averaged over the head, are low in comparison with other OMRI studies, where SAR values as high as 300 W kg⁻¹ averaged over the whole body are reported.^{45,52,53} Therefore, in future *in vivo* studies there is significant scope to increase B_{1e} in our OMRI probe, via increased EPR power, without concern for animal safety.

5 | CONCLUSION

We have detailed the design of an optimized OMRI platform that significantly mitigates the sensitivity challenges of ULF MRI and restricts RF power absorbance to levels that are safe for preclinical application. We note that, beyond the work presented here, our apparatus has proven robust during the study of more than 50 animals. We anticipate that the platform for time-resolved OMRI described here will enable systematic studies of ischemic stroke as well as other biological processes that can be probed with exogenous radicals.

ACKNOWLEDGEMENTS

We are grateful for the early technical contributions of Brandon D. Armstrong and Oliver Baltay. This research was supported by DOD DMRDP Award W81XWH-11-2-0076 (DM09094). D.E.J.W. was supported by ANSTO and the Australian-American Fulbright Commission. N.S. was supported by the Swiss National Science Foundation (P3000P2 147768).

ORCID

David E. J. Waddington  <http://orcid.org/0000-0002-7017-1556>

REFERENCES

1. Singh R, Devi S, Gollen R. Role of free radical in atherosclerosis, diabetes and dyslipidaemia: Larger-than-life. *Diabetes Metab Res Rev.* 2014;32:13-23.
2. Sanderson TH, Reynolds CA, Kumar R, Przyklenk K, Hüttemann M. Molecular mechanisms of ischemia-reperfusion injury in brain: Pivotal role of the mitochondrial membrane potential in reactive oxygen species generation. *Mol Neurobiol.* 2013;47:9-23.
3. Choudhari SK, Chaudhary M, Bagde S, Gadbaile AR, Joshi V. Nitric oxide and cancer: A review. *World J Surg Oncol.* 2013;11:118.
4. Epel B, Redler G, Halpern HJ. How in vivo EPR measures and images oxygen. *Adv Exp Med Biol.* 2014;812:113-119.
5. Danhier P, Gallez B. Electron paramagnetic resonance: A powerful tool to support magnetic resonance imaging research. *Contrast Media Mol Imaging.* 2015;10:266-281.
6. Lurie DJ, Bussell DM, Bell LH, Mallard JR. Proton-electron double magnetic resonance imaging of free radical solutions. *J Magn Reson.* 1988;76:366-370.
7. Golman K, Leunbach I, Ardenkjær-Larsen JH, et al. Overhauser-enhanced MR imaging (OMRI). *Acta Radiol.* 1998;39:10-17.
8. Utsumi H, Yamada K, Ichikawa K, Sakai K, Kinoshita Y, Matsumoto S. Simultaneous molecular imaging of redox reactions monitored by Overhauser-enhanced MRI with ¹⁴N- and ¹⁵N-labeled nitroxyl radicals. *Proc Natl Acad Sci USA.* 2006;103:1463-1468.
9. Ardenkjær-Larsen JH, Laursen I, Leunbach I, et al. EPR and DNP properties of certain novel single electron contrast agents intended for oximetric imaging. *J Magn Reson.* 1998;133:MN981438.
10. Halpern HJ, Chandramouli GVR, Barth ED, et al. Diminished aqueous microviscosity of tumors in murine models measured with in vivo radiofrequency electron paramagnetic resonance. *Cancer Res.* 1999;59:5836-5841.
11. He G, Samouilov A, Kuppusamy P, Zweier JL. In vivo imaging of free radicals: Applications from mouse to man. *Mol Cell Biochem.* 2002;234-235:359-367.
12. Kuppusamy P, Zweier JL. Cardiac applications of EPR imaging. *NMR Biomed.* 2004;17:226-239.
13. Vikram DS, Rivera BK, Kuppusamy P. In vivo imaging of free radicals and oxygen. *Methods Mol Biol.* 2010;610:3-27.
14. Lurie DJ, Davies GR, Foster MA, Hutchison JMS. Field-cycled PEDRI imaging of free radicals with detection at 450 mT. *Magn Reson Imaging.* 2005;23:175-181.
15. Subramanian S, Matsumoto K, Mitchell JB, Krishna MC. Radio frequency continuous-wave and time-domain EPR imaging and Overhauser-enhanced magnetic resonance imaging of small animals: Instrumental developments and comparison of relative merits for functional imaging. *NMR Biomed.* 2004;17:263-294.
16. Ahmad R, Kuppusamy P. Theory, instrumentation, and applications of electron paramagnetic resonance oximetry. *Chem Rev.* 2010;110:3212-3236.
17. Matsumoto S, Yamada K, Hirata H, et al. Advantageous application of a surface coil to EPR irradiation in Overhauser-enhanced MRI. *Magn Reson Med.* 2007;57:806-811.
18. Petryakov S, Samouilov A, Kesselring E, Caia GL, Sun Z, Zweier JL. Dual frequency resonator for 1.2 GHz EPR/16.2 MHz NMR co-imaging. *J Magn Reson.* 2010;205:1-8.
19. Sundramoorthy SV, Epel B, Halpern HJ. Orthogonal resonators for pulse in vivo electron paramagnetic imaging at 250 MHz. *J Magn Reson.* 2014;240:45-51.
20. Neudert O, Raich HP, Mattea C, Stapf S, Münnemann K. An Alderman-Grant resonator for S-band dynamic nuclear polarization. *J Magn Reson.* 2014;242:79-85.
21. Sarracanie M, Armstrong BD, Stockmann J, Rosen MS. High speed 3D Overhauser-enhanced MRI using combined b-SSFP and compressed sensing. *Magn Reson Med.* 2013;71:735-745.
22. Koonjoo N, Parzy E, Massot P, et al. In vivo Overhauser-enhanced MRI of proteolytic activity. *Contrast Media Mol Imaging.* 2014;9:363-371.
23. Sarracanie M, Lapierre CD, Salameh N, Waddington DEJ, Witzel T, Rosen MS. Low-cost high-performance MRI. *Sci Rep.* 2015;5:15177.
24. Salameh N, Sarracanie M, Armstrong BD, Rosen MS, Comment A. Overhauser-enhanced magnetic resonance elastography. *NMR Biomed.* 2016;29:607-613.
25. Sun Z, Li H, Petryakov S, Samouilov A, Zweier JL. In vivo proton electron double resonance imaging of mice with fast spin echo pulse sequence. *J Magn Reson.* 2012;35:471-475.
26. Deng-Bryant Y, Singh IN, Carrico KM, Hall ED. Neuroprotective effects of tempol, a catalytic scavenger of peroxynitrite-derived free radicals, in a mouse traumatic brain injury model. *J Cereb Blood Flow Metab.* 2008;28:1114-1126.
27. Behringer W, Safar P, Kentner R, et al. Antioxidant Tempol enhances hypothermic cerebral preservation during prolonged cardiac arrest in dogs. *J Cereb Blood Flow Metab.* 2002;22:105-117.
28. Lochhead JJ, McCaffrey G, Quigley CE, Finch J, DeMarco KM, Nametz N, Davis TP. Oxidative stress increases blood-brain barrier permeability and induces alterations in occludin during hypoxia-reoxygenation. *J Cereb Blood Flow Metab.* 2010;30:1625-1636.
29. Jin H, Kanthasamy A, Ghosh A, Anantharam V, Kalyanaraman B, Kanthasamy AG. Mitochondria-targeted antioxidants for treatment of Parkinson's disease: Preclinical and clinical outcomes. *Biochim Biophys Acta.* 2014;1842:1282-1294.
30. Tsai LL, Mair RW, Rosen MS, Patz S, Walsworth RL. An open-access, very-low-field MRI system for posture-dependent ³He human lung imaging. *J Magn Reson.* 2008;193:274-285.
31. Gilbert KM, Scholl TJ, Chronik BA. RF coil loading measurements between 1 and 50 MHz to guide field-cycled MRI system design. *Concept Magn Reson B.* 2008;33B:177-191.
32. Coffey AM, Kovtunov KV, Barskiy DA, et al. High-resolution low-field molecular magnetic resonance imaging of hyperpolarized liquids. *Anal Chem.* 2014;86:9042-9049.
33. Haacke EM, Brown RW, Thompson MR, Venkatesan R. *Magnetic Resonance Imaging: Physical Principles and Sequence Design.* New York: Wiley-Liss; 1999.

34. Alderman DW, Grant DM. An efficient decoupler coil design which reduces heating in conductive samples in superconducting spectrometers. *J Magn Reson.* 1979;36:447-451.
35. Mispelter J, Mikaela L, Briguet A. *NMR Probeheads for Biophysical and Biomedical Experiments.* London: Imperial College Press; 2006.
36. Doty FD, Entzminger G, Kulkarni J, Pamarthy K, Staab JP. Radio frequency coil technology for small-animal MRI. *NMR Biomed.* 2007;20:304-325.
37. Li S, Yang QX, Smith MB. RF coil optimization: Evaluation of B_1 field homogeneity using field histograms and finite element calculations. *Magn Reson Imaging.* 1994;12:1079-1087.
38. Gabriel S, Lau RW, Gabriel C. The dielectric properties of biological tissues: II. Measurements in the frequency range 10 Hz to 20 GHz. *Phys Med Biol.* 1996;41:2251-2269.
39. Armstrong BD, Han S. A new model for Overhauser enhanced nuclear magnetic resonance using nitroxide radicals. *J Chem Phys.* 2007;124:104508:127.
40. Sarracanie M, Herisson F, Salameh N, Ayata C, Rosen MS. A marker for hyperacute ischemic stroke at ultra-low magnetic field. In: Proceedings of the 24th Annual Meeting ISMRM; 2016; Singapore. 1440.
41. Escobales N, Nuñez RE, Jang S, et al. Mitochondria-targeted ROS scavenger improves post-ischemic recovery of cardiac function and attenuates mitochondrial abnormalities in aged rats. *J Mol Cell Cardiol.* 2014;77:136-146.
42. Krainz T, Gaschler MM, Lim C, Sacher JR, Stockwell BR, Wipf P. A mitochondrial-targeted nitroxide is a potent inhibitor of ferroptosis. *ACS Cent Sci.* 2016;2:653-659.
43. Sowers MA, McCombs JR, Wang Y, et al. Redox-responsive branched-bottlebrush polymers for in vivo MRI and fluorescence imaging. *Nat Commun.* 2014;5:1-9.
44. Eaton GR, Eaton SS, Barr DP, Weber RT. *Quantitative EPR.* New York; Springer; 2010.
45. Krishna MC, English S, Yamada K, et al. Overhauser enhanced magnetic resonance imaging for tumor oximetry: Coregistration of tumor anatomy and tissue oxygen concentration. *Proc Natl Acad Sci USA.* 2002;99:2216-2221.
46. Waddington DEJ, Sarracanie M, Zhang H, et al. Nanodiamond-enhanced MRI via in situ hyperpolarization. *Nat Commun.* 2017;8:15118.
47. Darrasse L, Ginefri JC. Perspectives with cryogenic RF probes in biomedical MRI. *Biochimie.* 2003;85:915-937.
48. Baudin E, Safiullin K, Morgan SW, Nacher PJ. An active feedback scheme for low field NMR experiments. *J Phys Conf Ser.* 2011;012009:294.
49. Hoult DI, Lauterbur PC. The sensitivity of the zeugmatographic experiment involving human samples. *J Magn Reson.* 1979;34:425-433.
50. Petryakov S, Samouilov A, Chzhan-Roytenberg M, Kesselring E, Sun Z, Zweier JL. Segmented surface coil resonator for in vivo EPR applications at 1.1 GHz. *J Magn Reson.* 2009;198:8-14.
51. Enomoto A, Emoto M, Fujii H, Hirata H. Four-channel surface coil array for sequential CW-EPR image acquisition. *J Magn Reson.* 2013;234:21-29.
52. Matsumoto S, Yasui H, Batra S, et al. Simultaneous imaging of tumor oxygenation and microvascular permeability using Overhauser enhanced MRI. *Proc Natl Acad Sci USA.* 2009;106:17898-17903.
53. Massot P, Parzy E, Pourtau L, et al. In vivo high-resolution 3D Overhauser-enhanced MRI in mice at 0.2 T. *Contrast Media Mol Imaging.* 2012;7:45-50.

SUPPORTING INFORMATION

Additional Supporting Information may be found online in the supporting information tab for this article.

How to cite this article: Waddington DEJ, Sarracanie M, Salameh N, Herisson F, Ayata C, Rosen MS. An Overhauser-enhanced-MRI platform for dynamic free radical imaging *in vivo*. *NMR in Biomedicine.* 2018; e3896. <https://doi.org/10.1002/nbm.3896>